Observations of Wall Cloud Formation in Supercell Thunderstorms during VORTEX2

NOLAN T. ATKINS, EVA M. GLIDDEN, AND TIMOTHY M. NICHOLSON

Department of Atmospheric Sciences, Lyndon State College, Lyndonville, Vermont

(Manuscript received 18 August 2014, in final form 7 August 2014)

ABSTRACT

This study presents an integrated analysis of dual-Doppler, cloud photogrammetry, surface mobile mesonet, and sounding data to examine wall cloud formation in two supercells observed during the Verification of the Origins of Rotation in Tornadoes Experiment II (VORTEX2). One of the wall clouds contained significant rotation and spawned an (enhanced Fujita) EF2 tornado, while the other was clearly displaced horizontally from the mesocyclone and exhibited little rotation at the time of data collection. Backward parcel trajectories show that the majority of the air entering the wall cloud base originates in the forward-flank region. A small fraction of the parcels enter the wall cloud base from the inflow. Some rear-flank downdraft parcels descend into the strongly rotating wall cloud. For both wall clouds, much of the observed wall cloud lowering is attributed to evaporatively cooled parcels in the forward-flank region being ingested into the low-level updraft. Additional wall cloud-base lowering is observed near the circulation center of the strongly rotating wall cloud. This localized lowering is created by the pressure deficit and associated cooling. The observational results presented herein are compared to long-standing wall cloud formation conceptual models published in the refereed literature.

1. Introduction

The wall cloud is a lowering of cloud base associated with the updraft of a thunderstorm. The focus of this study concerns wall clouds formed within supercell thunderstorms (Bluestein 1983; Davies-Jones 1986; Bluestein 1993). Early observational studies suggest that the supercell wall cloud is the visual indicator of a strong updraft core and may exhibit cyclonic rotation. (Moller 1978; Bluestein 1984). Recent studies have also revealed the existence of anticyclonic wall clouds (Atkins et al. 2012) that may be associated with anticyclonic circulations in the hook region that have been well documented in the literature (see references in Markowski 2002; Markowski et al. 2008). National Weather Service storm spotter training documents indicate that persistent wall clouds developing strong rotation and exhibit rapid upward vertical motion are often regarded as precursors to tornadogenesis (http://www.crh.noaa.gov/dmx/presentations/spotter-training/NWS-Spotter-Training_files/v3_document.htm). While many studies of supercell thunderstorms have photodocumented the wall cloud, little is known about their formation.

Our current understanding of wall cloud formation is based on idealized modeling results of Rotunno and Klemp (1985, hereafter RK85) and visual observations. In their idealized simulation of a supercell, RK85 show that midlevel parcels with low equivalent potential temperature (θ_e) descend to the low-level (within a few hundred meters above ground) forward-flank region. The parcels then move toward and subsequently ascend into the dynamically forced (Rotunno and Klemp 1982; RK85) low-level updraft. In doing so, these low θ_e parcels saturate at a lower altitude relative to the primary cloud base, forming the wall cloud. Observations by storm intercept teams have since confirmed that cloud elements associated with cooler air behind the gust front often rise into the updraft. Often this occurs near or in association with the distinct "tail cloud" that protrudes from near the base of the wall cloud toward the cooler air. This mechanism is described in National Weather Service storm spotter training documents (http://www.nws.noaa.gov/training/wxspot.php).

To our knowledge, no observational study has confirmed the RK85 mechanism for wall cloud formation. It

Corresponding author address: Nolan T. Atkins, Department of Atmospheric Sciences, Lyndon State College, 1001 College Rd., Lyndonville, VT 05851.
E-mail: nolan.atkins@lyndonstate.edu

DOI: 10.1175/MWR-D-14-00125.1

is not known what fraction of air creating observed wall clouds originates in the storm midlevels or from other source regions such as the inflow. Given that some wall clouds may be collocated with the low-level mesocyclone[1] and, therefore, contain significant low-level rotation, it is possible that some of the wall cloud lowering is created by the pressure deficit and attendant cooling at the circulation center. While this mechanism may not explain all of the lowering for wall clouds associated with weak rotation, it may explain a significant portion of the lowering associated with strongly rotating wall clouds. No study has systematically examined this wall cloud formation mechanism.

The objective of this study is to examine wall cloud formation mechanisms within supercell thunderstorms. The requisite visual, kinematic, and thermodynamic data to examine the aforementioned wall cloud formation mechanisms was collected during the Verification of the Origins of Rotation in Tornadoes Experiment II (VORTEX2). VORTEX2 was a large multiagency field project designed to collect observations in and around supercell thunderstorms. To increase the number of storm intercepts, the experiment was mobile covering the southern, central, and northern plains states during the spring seasons of 2009 and 2010. More information concerning VORTEX2 can be found in the summary article by Wurman et al. (2012).

Analyses of two supercells observed during VORTEX2 are presented herein. The first formed on 5 June 2009 over Goshen County, Wyoming (hereafter referred to as the Goshen County supercell). This supercell produced a well-defined wall cloud and attendant (enhanced Fujita) EF2 tornado. The second supercell occurred on 11–12 June 2009 west-northwest of La Junta, Colorado (hereafter referred to as the La Junta supercell). While this supercell was tornado warned during the time of VORTEX2 data collection, it did not spawn a tornado despite producing a well-defined wall cloud.

This paper is organized as follows. Section 2 discusses the data and analysis methods employed. Section 3 presents results for the two aforementioned supercells while a discussion and summary are given in section 4.

2. Data analysis methodology

a. Radar data

The wind fields in and around the wall clouds were generated from dual-Doppler syntheses of radial velocities collected by the mobile X-band Doppler on Wheels (DOW) 6 and 7 radars operated by the Center for Severe Weather Research (CSWR; Wurman 2001). The dual-Doppler methodology employed in this study follows those used in Atkins et al. (2012), Markowski et al. (2012a,b), and Kosiba et al. (2013). The interested reader can find the analysis details in the appendix.

b. Mobile mesonet

The thermodynamic properties of low-level (within the lowest few hundred meters above ground) parcels entering the wall cloud are based on mobile mesonet (Straka et al. 1996; Waugh and Fredrickson 2010) observations. The mobile mesonets carried roof-mounted instrumentation that recorded time, latitude, longitude, pressure, temperature, relative humidity, and wind velocity. All data were collected at 1-s intervals. Higher-frequency noise is filtered out with a triangular weight with filter radius of 5 s. Data collected within the window of 6 min before and after the center dual-Doppler analysis time are used in the analyses. While we acknowledge that the storm is evolving during the 12-min time period, it is assumed that the thermodynamic characteristics within the hook region do not considerably change. Temperature data collected at times when the vehicles were at rest and wind data during significant accelerations, however, are not used. All mobile mesonet data are space–time adjusted to account for storm motion.

c. Photogrammetry

The spatial extent and evolution of the wall clouds is determined by photogrammetric analysis of still images captured by two photo teams. Photogrammetry is the process of extracting quantitative information from a photograph, such as the horizontal and vertical extent of a wall cloud, by superimposing azimuth and elevation angle grids. To generate the grid, the precise azimuths of landmarks in the horizon relative to the photographer must be measured or computed. Once the landmark locations are known, the effective focal length and tilt angle of the photograph can be computed. Spherical trigonometry is then used to create the azimuth–elevation grid. A gridded photo can then be combined with the dual-Doppler wind field and radar reflectivity observations. It is also possible to use contemporaneous photographs taken at the two photographer positions to triangulate wall cloud positions. Once the wall cloud location is known, the vertical extent can be photogrammetrically computed. A general discussion of photogrammetry can be found in Abrams (1952), Holle (1986), and Zehnder et al. (2007) or specifically for the Goshen County supercell in Wakimoto et al. (2011) and Atkins et al. (2012).

[1] The low-level mesocyclone is often observed at altitudes of 0–3 km above ground level.

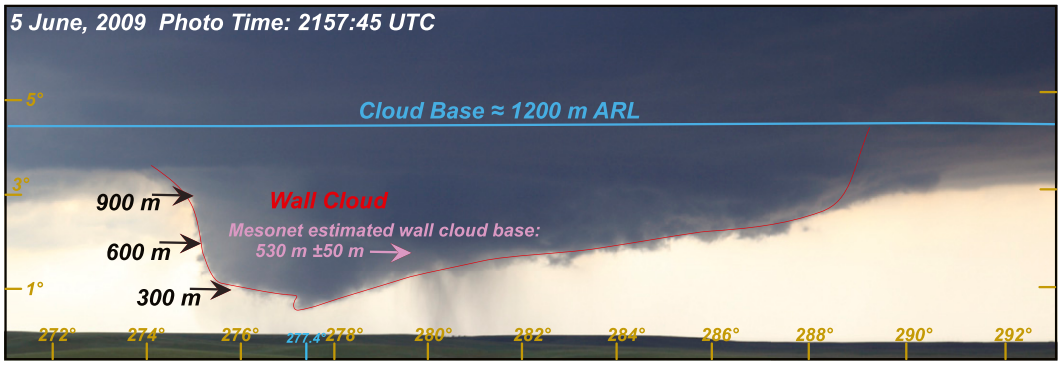

FIG. 1. Photograph of the wall cloud taken at 2157:45 UTC 5 Jun 2009. Estimates of cloud-base height from the sounding in Fig. 7 (blue) and the wall cloud vertical extent based on photogrammetry (black) are shown. Mobile mesonet estimated wall cloud-base height is shown in pink. Wall cloud boundary is shown in red.

3. Wall cloud formation

a. Goshen County tornadic wall cloud

1) VISUAL AND DUAL-DOPPLER OBSERVATIONS

The Goshen County tornadic supercell has been the focus of many studies (Wakimoto et al. 2011; Atkins et al. 2012; Markowski et al. 2012a,b; Richardson et al. 2012; Kosiba et al. 2013; Wakimoto et al. 2012; Wurman et al. 2013; French et al. 2014; Marquis et al. 2014) because of the comprehensive, high spatial and temporal resolution data collected by numerous ground teams. A wall cloud was observed with the Goshen County supercell as the VORTEX2 teams arrived to the deployment area at approximately 2125 UTC. The Goshen supercell was in the "tornadogenesis" phase (Kosiba et al. 2013) from 2150 to 2202 UTC. A radar-detected tornado formed at about 2152 UTC but was not yet visible.

The wall cloud at 2157:45 UTC is shown in Fig. 1 where the view is from the DOW7 location on Highway 85 looking to the west [see Fig. 1 in Wakimoto et al. (2011) for the radar and photo team locations relative to the hook echo]. The wall cloud is approximately 17 km from the radar/photo location. The wall cloud lowering is centered on azimuths 276°–278° and extended nearly 900 m below the primary cloud base of 1200 m above radar level (ARL; relative to DOW 7). The primary cloud base is determined photgrammetrically and with a nearby inflow sounding (shown later). The wall cloud lowering is asymmetric as it is gradually higher to the north. Rain curtains are observed to the north and south of the wall cloud suggesting that it is embedded within precipitation. The location of the wall cloud relative to the hook echo is shown in Fig. 2. Consistent with Fig. 1, the wall cloud is embedded in precipitation that was wrapping around and embedded in the low-level mesocyclone (Fig. 2a). Video (not shown) reveals that the wall cloud contained significant rotation. The strongest rotation in the dual-Doppler data is located by computing the minimum Okubo–Weiss number (Okubo 1970; Weiss 1991; Markowski et al. 2011). It is located at an azimuth of 277.4° from the DOW7/photo location (Fig. 2) near the wall cloud center. The lowest portion of the wall cloud is located at the same azimuth (Fig. 1).

It has long been accepted and shown by RK85 that the wall cloud is embedded within low-level updraft. The updraft is necessary to dynamically force the evaporatively cooled, negatively buoyant air to the wall cloud base (Rotunno and Klemp 1982; RK85). The wall cloud position relative to the vertical velocity field in Fig. 2b suggests that the wall cloud is on the gradient of vertical velocity and contains some downdraft on the southern and eastern flanks. This downdraft air is associated with the rear-flank downdraft (RFD) that is wrapping around and occluding the wall cloud. Examination of video (not shown) shows cloud elements on the southern periphery of the wall cloud descending and dissipating at the times shown in Figs. 1–4. A secondary rear-flank gust front (SRFGF) is also observed to the south of the wall cloud. While the RFD has long been thought to play a role in tornadogenesis (e.g., Lemon and Doswell 1979), recent studies have also focused on the SRFGF (Wurman et al. 2007; Grzych et al. 2007; Marquis et al. 2008; Finley et al. 2010; Wurman et al. 2010; Lee et al. 2011; Kosiba et al. 2013) impacting the production, distribution, and amplification of low-level vorticity near the developing tornado.

Similar results are observed a couple minutes later with photos taken at 2200:24 and 2200:33 UTC at the DOW7 and DOW6 locations, respectively. Much of the wall cloud base is found at about 560 m ARL (Fig. 3a). An additional 180 m of lowering is observed just north of the wall cloud center. It is possible to triangulate the wall

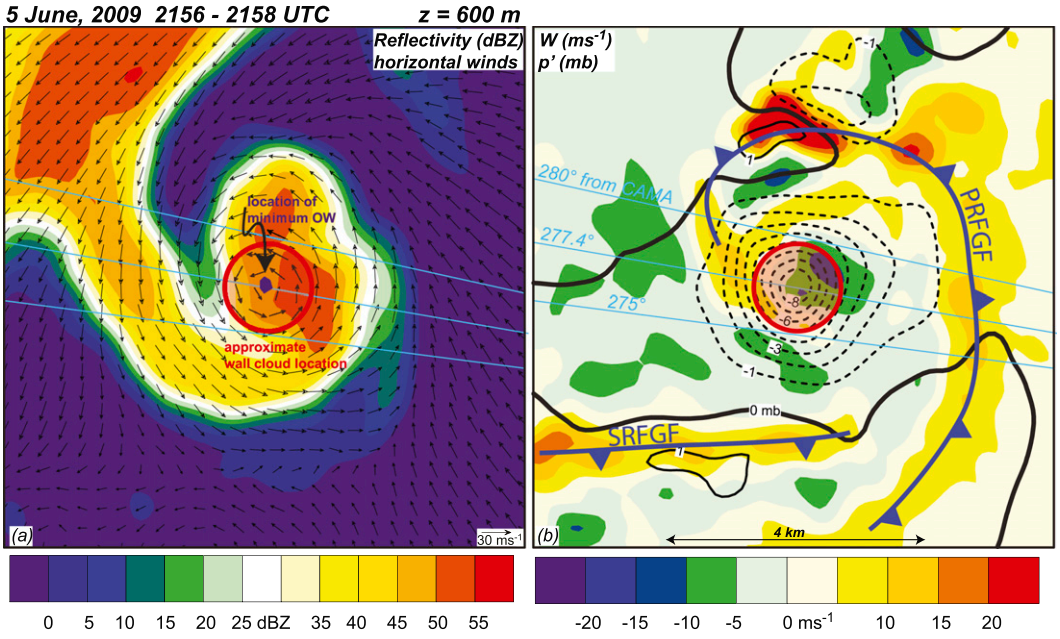

FIG. 2. Dual-Doppler data from 2156:00 to 2158:00 UTC at 600 m ARL are shown. (a) Radar reflectivity from DOW 7 (color) and storm-relative winds ($m\,s^{-1}$; black vectors). Cyan lines are the left, center, and right azimuths of the estimated wall cloud location based on photogrammetry. The thick red line is the approximate wall cloud location. The location of minimum Okubo–Weiss number is filled purple. (b) Vertical velocity ($m\,s^{-1}$; color) and perturbation pressure (black contours) are shown. In (b), the wall cloud location and azimuths are as in (a). Approximate locations of the primary rear-flank gust front (PRFGF) and secondary rear-flank gust front (SRFGF) are shown in blue.

cloud location in Fig. 3 and superimpose the position on the radar data collected from 2200 to 2202 UTC. As shown in Fig. 4 and consistent with the results in Fig. 2, the wall cloud is located in a region of precipitation associated with the hook echo and appears to be located within the low-level mesocyclone. Notice that the strongest rotation is not located at the center of the wall cloud. Rather, it is displaced to the north and is collocated with the local wall cloud lowering shown in Fig. 3. This is the location of the developing tornado. DOW7 single-Doppler velocities within the rotational couplet are increasing from 2159 to 2202 UTC. The condensation funnel made visual contact with the ground at about 2206 UTC (Wakimoto et al. 2011; Atkins et al. 2012). As in Fig. 2b, the wall cloud at 2200 UTC is located on the gradient of vertical velocity (Fig. 4b).

2) WALL CLOUD PARCEL SOURCE REGIONS

To test the wall cloud formation hypothesis put forth by RK85, it is necessary to identify regions of the storm from which parcels entering the wall cloud base are coming from. This is accomplished by calculating backward parcel trajectories for hundreds of parcels arriving at the wall cloud base at 550 m ARL. Trajectories are computed for 10 min beginning at 2200 UTC. Results of this analysis are shown in Fig. 5 for the wall cloud observed at 2200 UTC in Fig. 3.[2] The trajectories in Figs. 5a,c illustrate that parcels entering the wall cloud come from one primary and two secondary source regions. The primary source region is the forward flank. The two secondary source regions are the inflow and rear-flank downdraft. The inflow parcels originate at low levels, wrapping around the northern and western flanks before entering the wall cloud (Figs. 5b,d). A few of the inflow parcels ascend over the primary rear flank gust front (PRFGF) before descending into the wall cloud. It was somewhat surprising to observe parcels reaching the wall cloud base that have descended in downdraft. A few parcels descend within the rear-flank downdraft while others originate in the forward-flank region at altitudes greater than 1000 m ARL and then descend to the wall cloud base (Fig. 5b). It is possible that errors inherent in the dual-Doppler analysis and trajectory calculations are creating erroneous parcel paths. The descending parcels, however, are consistent with the wall cloud located in a gradient of vertical velocity (Figs. 2

[2] Trajectories were also computed entering the wall cloud in Fig. 1, but are not shown since the results are nearly identical to those in Fig. 5.

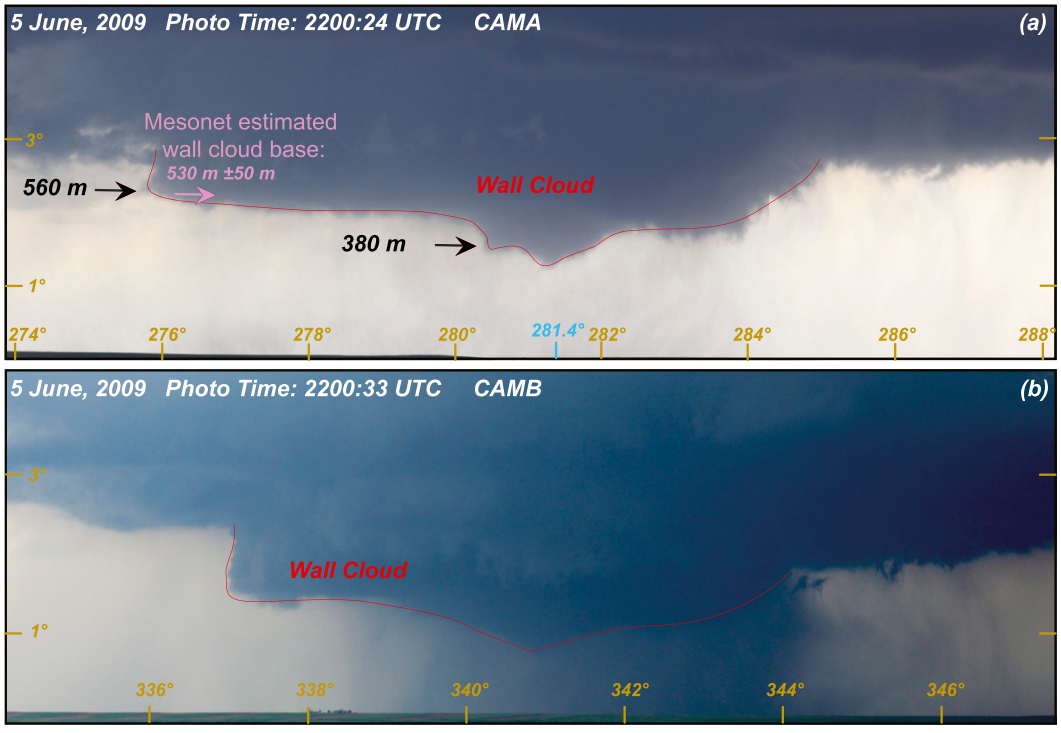

FIG. 3. Photographs of the wall cloud taken at (a) 2200:24 UTC from the CAMA and (b) 2200:33 UTC from the CAMB locations, respectively on 5 Jun 2009. Photogrammetric and mobile mesonet estimates of the wall cloud-base height are shown in black and pink, respectively. The wall cloud boundary is shown in red.

and 4) and video showing descending cloud elements on the southern periphery of the wall cloud (not shown). The majority of the forward-flank parcels originate at low levels (Figs. 5b,d) and ascend to the wall cloud base in a manner consistent with the idealized modeling results of RK85. The low-level forward flank trajectories in Fig. 5 are also consistent with those shown by Kosiba et al. (2013) entering the low-level mesocyclone.

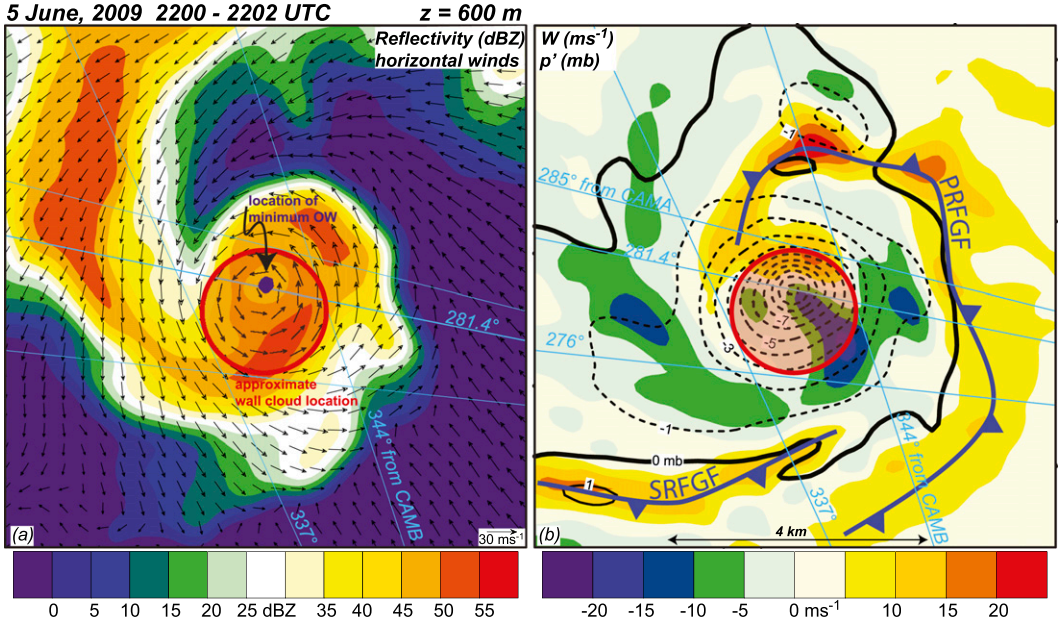

FIG. 4. As in Fig. 2, but for the time period 2200:00–2202:00 UTC.

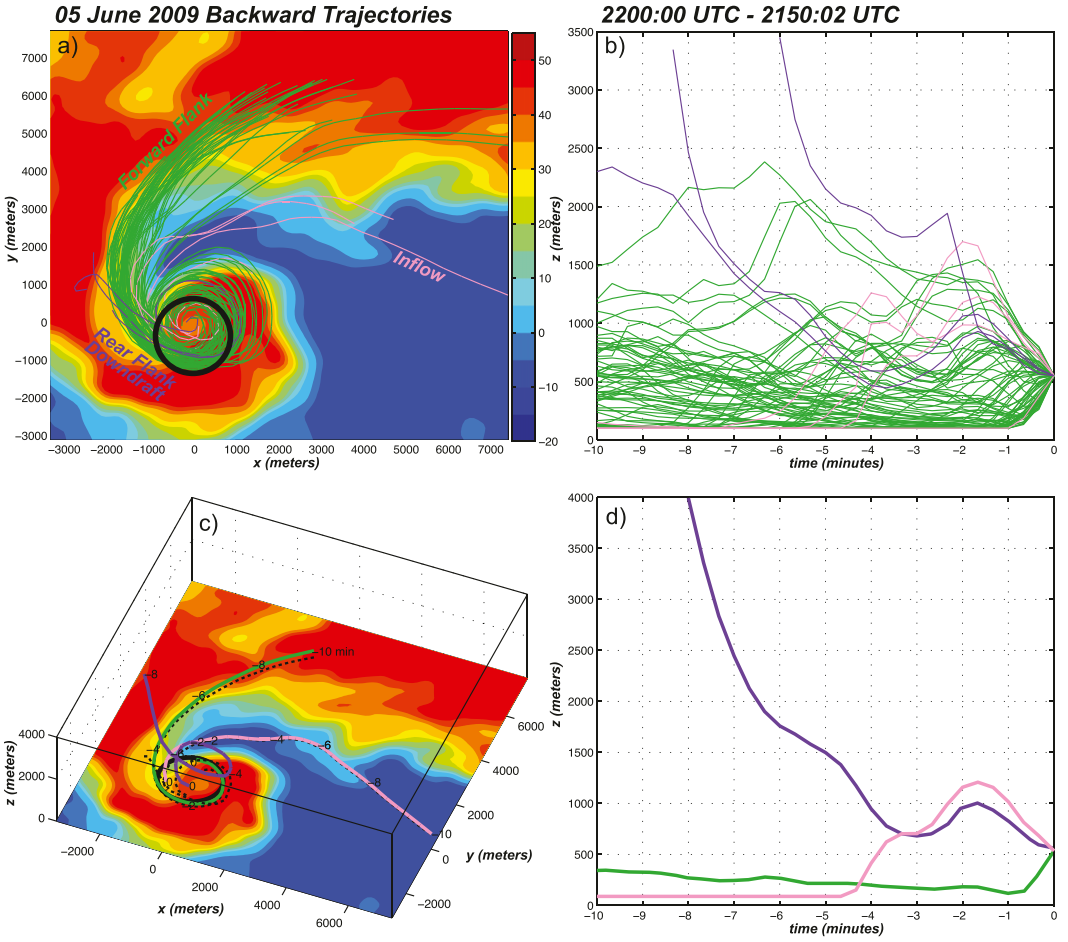

FIG. 5. Radar reflectivity from DOW 7 (color; 300 m ARL) and backward trajectories for parcels entering the wall cloud. Trajectories were started at 550 m ARL. The radar reflectivity data are from the 2200:00–2202:00 dual-Doppler analysis. Backward trajectories were calculated from 2200:00 to 2150:00 UTC. (a) Plan view of radar reflectivity and trajectories. Inflow, forward-flank, and rear-flank downdraft parcels are colored pink, green, and purple, respectively. The approximate wall cloud location is shown in black. (b) Height vs time plot of the trajectories shown in (a). (c) Three-dimensional perspective of the radar reflectivity field shown in (a) along with representative parcel trajectories from the inflow, forward-flank, and rear-flank downdraft locations. Black dashed lines represent the ground-relative location of the respective trajectories. Black time labels are minutes before the initial time of 2200:00 UTC. (d) Height vs time diagram of the three representative trajectories shown in (c).

3) WALL CLOUD FORMATION

Wall cloud formation is now examined and compared to the long-standing model put forth by RK85. Recall that much of the air entering the wall cloud base originates in the low-level forward-flank region. The thermodynamic properties of this air are reasonably approximated with the mobile mesonet data (Fig. 6) despite the sparse coverage in and around the hook echo due to the limited road network over southeastern Wyoming. The rear- and forward-flank regions are about 3–4 K cooler and about 1 g kg^{-1} moister than the inflow (Figs. 6 and 7). The virtual potential temperature deficit of the storm's downdraft regions is approximately 3 K (Kosiba et al. 2013). While direct comparison is not appropriate, it is worth mentioning that the low-level forward-flank air in the RK85 idealized modeling study is approximately 7 K cooler and 1 g kg^{-1} drier than the ambient flow. Using all available mobile mesonet data in the forward-flank region where wall cloud parcels came from (gray shaded region in Fig. 6), the mean potential temperature and mixing ratios are calculated and shown in the inset diagram of Fig. 7.[3] Assuming hydrostatic adiabatic ascent, these low-level forward-flank parcels will saturate at approximately 530 m ARL (Fig. 7). This altitude is

[3] Not all of the mobile mesonet data are shown in Fig. 6 for figure clarity.

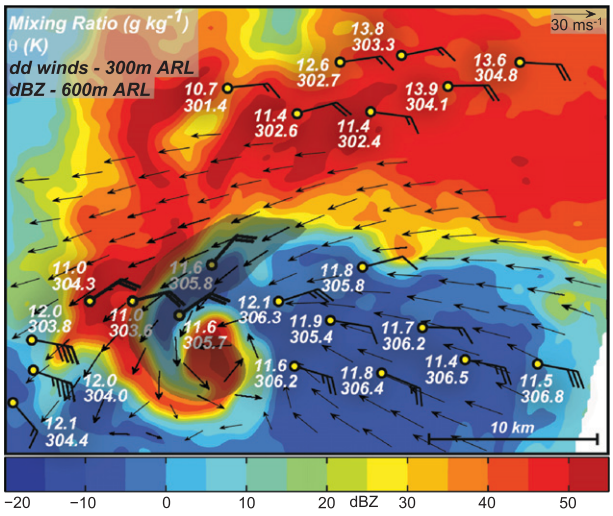

FIG. 6. Radar reflectivity from DOW 7 (color; 600 m ARL) and dual-Doppler winds (black vectors; 300 m ARL) from 2156:00 to 2158:00 UTC. Mobile mesonet winds (black barbs; ½ flag = 5 m s^{-1}, full flag = 10 m s^{-1}), mixing ratio (g kg^{-1}), and potential temperature (K) are shown from 2150:00 to 2202:00 UTC. The semitransparent region represents the location of forward-flank parcel trajectories shown in Fig. 5.

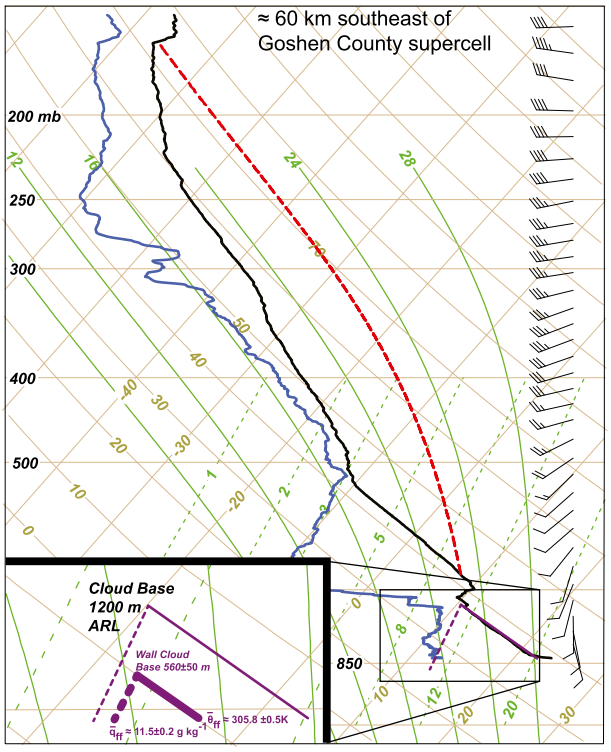

FIG. 7. NCAR GAUS sounding launched at 2155:22 UTC 5 Jun 2009 approximately 60 km to the southeast of the Goshen County tornadic supercell. Red dashed line is the lifted parcel path. Half and full wind barbs are 5 and 10 m s^{-1}, respectively. The inset cloud-base height is based on the sounding data. The wall cloud-base estimate is calculated from mobile mesonet observations in the forward-flank region.

nearly identical to the observed wall cloud base of 560 m ARL at 2200:24 and 2200:33 UTC (Fig. 3) and is within the range of 300–900 m ARL for the sloping wall cloud at 2157:45 UTC. It is acknowledged that direct comparison of an instantaneous photograph with dual-Doppler data collected over a period of 2 min can, at times, be challenging because of the nearly continuous storm evolution.

Apparent in Fig. 3a is the localized lowering just north of the wall cloud center. This lowering is evident in Fig. 3a between azimuths of 280° and 282°. It extends about 180 m below the primary wall cloud base. It is hypothesized that this lowering is associated with a nonhydrostatic dynamic pressure deficit associated with the rotation in the wall cloud. A pressure retrieval from the dual-Doppler wind field was performed using techniques established by Gal-Chen (1978) and Hane and Ray (1985). The perturbation pressure fields are shown in Figs. 2b and 4b for the 2156–2158 and 2200–2202 UTC volume scans, respectively. In Fig. 2b, the lowest pressure perturbation is approximately −8 mb (1 mb = 1 hPa) and was centered on an azimuth of 277.4°. The lowest extent of the wall cloud is observed at 2257:45 UTC at this same azimuth (Fig. 1). The pressure perturbation in Fig. 4b is about −10 mb, centered on 281.4°. The localized lowering in Fig. 4b is located between azimuths of 280° and 282°. An independent ground-based velocity track display (GBVTD) analysis of the radar data shown in Figs. 2 and 4 produces nearly identical pressure deficits at the circulation center (not shown). Thus, the lowest portion of the wall cloud base is collocated with the lowest pressure.

An analysis was performed to determine if the pressure and associated temperature deficits may lead to additional wall cloud lowering. The linearized form of the ideal gas law discussed in Bannon (2002) is used for this analysis. The base state is assumed to be dry, in hydrostatic balance, and satisfies the ideal gas law. Because the base state is dry, all moist variables are included in the perturbations. The linearized ideal gas law can be written as

$$\frac{p'}{p_{as}} = \frac{\rho'_a}{\rho_{as}} + \frac{T'}{T_s} + \frac{r_v}{\varepsilon}, \tag{1}$$

where p', ρ', and T' are the perturbations from the base state of pressure, density, and temperature, respectively. The subscripts a and s refer to dry air and the base state, respectively; r_v is the water vapor mixing ratio; and $\varepsilon = 0.622$. The pressure perturbation can be written as $p' = p_d + e$, where p_d is the nonhydrostatic dynamic

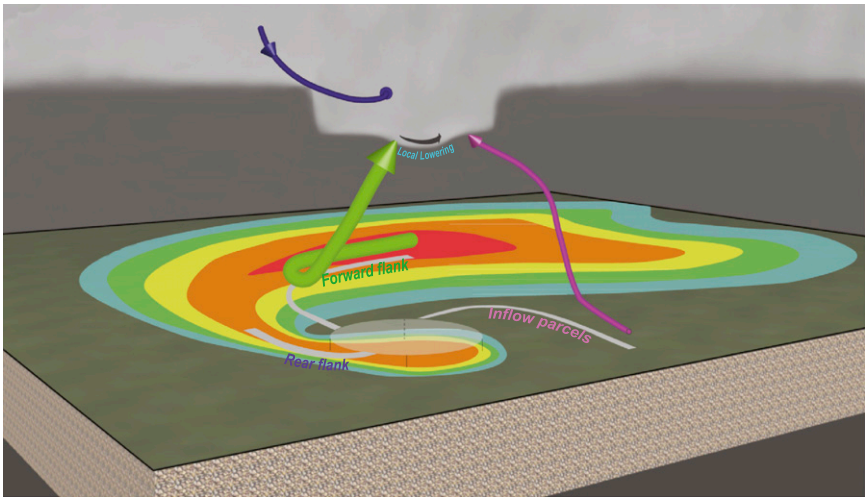

FIG. 8. Schematic diagram illustrating wall cloud formation within the Goshen County supercell on 5 Jun 2009. Color fill contours are radar reflectivity. The cloud and wall cloud are shaded gray. Parcels entering the wall cloud from the forward-flank, inflow, and rear-flank downdraft are shown as green, pink, and purple arrows, respectively. The percentage of air entering the wall cloud and importance of the respective source regions are indicated by the arrow thickness. The near-surface parcel paths are shown as gray lines. The projected location of the wall cloud near the surface is also shown in gray. The local lowering is a region of strong rotation within the wall cloud.

pressure perturbation within the wall cloud and e is the vapor pressure. The dynamic pressure deficit within the wall cloud is created by the large curvature and shear (Klemp and Rotunno 1983; RK85) in the horizontal wind field. Assuming that $\rho_a'/\rho_{as} \approx 0$ and neglecting moisture, Eq. (3) can be used to estimate T', the temperature deficit associated with the pressure drop within the rotating wall cloud. Using data from the inflow sounding in Fig. 7, the values of T_s and p_{as} are approximately 17.0°C and 777.5 hPa at the wall cloud base. The dynamic pressure deficit within the wall cloud can be estimated from the retrieved pressure field in Fig. 4.

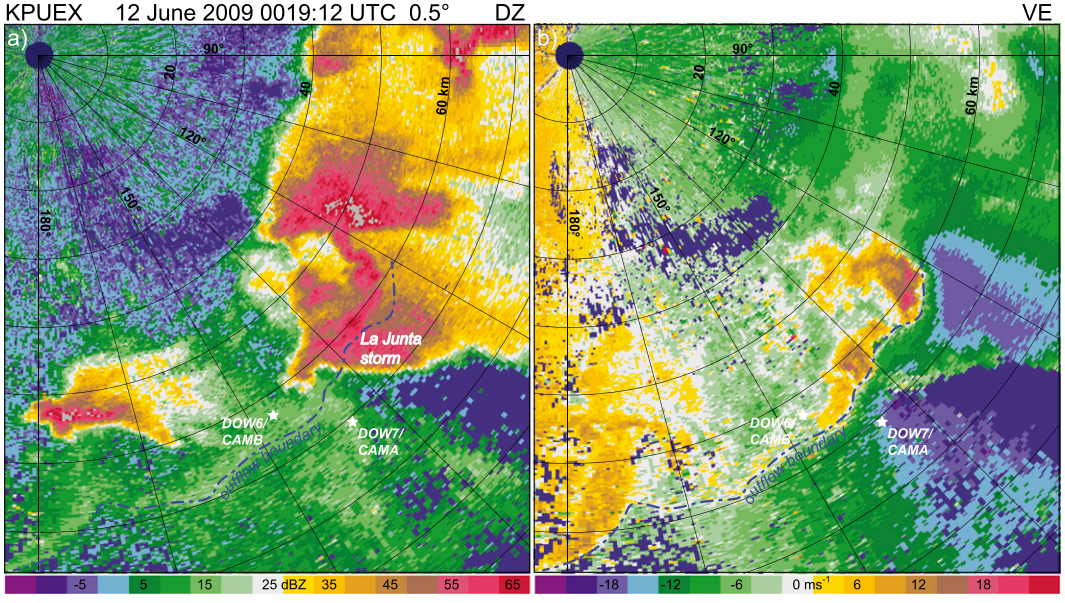

FIG. 9. WSR-88D data from Pueblo, CO (KPUEX), radar. (a) Radar reflectivity (dBZ) and (b) radial velocities ($m\,s^{-1}$) from the 0.5° elevation scan. The locations of the La Junta supercell, DOW6/CAMB, and DOW7/CAMA are all indicated. The outflow boundary is delineated with the blue dashed–dotted line.

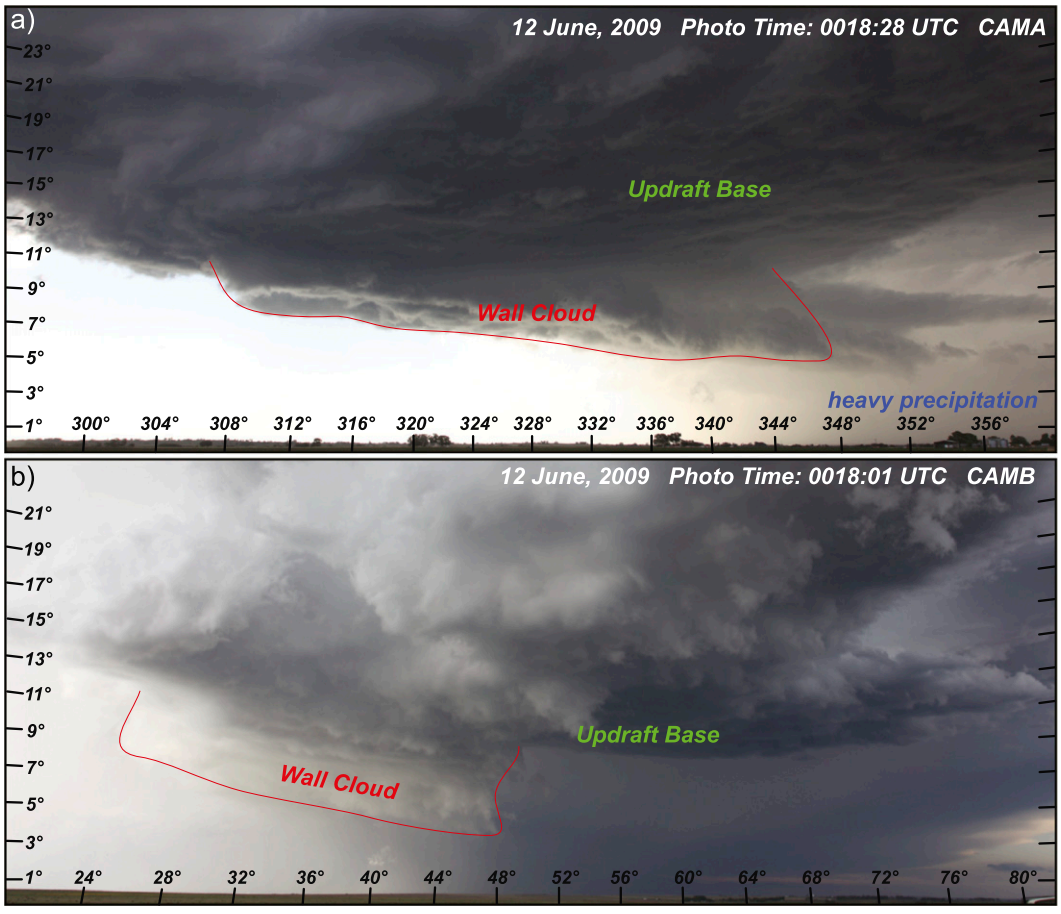

FIG. 10. Photographs of the La Junta supercell wall cloud taken at 0018:28 and 0018:01 UTC 12 Jun 2009 at the CAMA (collocated with DOW7) and CAMB (collocated with DOW6) locations, respectively, shown in Fig. 9. The approximate wall cloud boundary is shown in red.

Within the wall cloud, the pressure drops by approximately 6–7 hPa from the periphery to the location of lowest pressure. Plugging these values into Eq. (3) results in approximately 2.2°C of cooling. Assuming a constant mixing ratio below the wall cloud base, a cooling of 2.2°C results in a lowering of the cloud base to approximately 290 m ARL. This is lower than the photogrammetric estimate of 380 m ARL. It should be noted that the localized lowering was visually observed closer to the ground after 2200:24 UTC with a brief funnel forming at 2202:33 UTC. Given the uncertainties in the calculations and transient nature of the wall cloud base, it is argued that the localized lowering is consistent with what would be produced by the pressure deficit observed within the wall cloud.

A schematic diagram summarizing wall cloud formation within the Goshen County supercell observed on 5 June 2009 is shown in Fig. 8. It highlights the importance of rain-cooled air originating in the forward-flank region of the storm ascending in low-level updraft thereby saturating below the primary cloud base. Additional lowering may be associated with the nonhydrostatic pressure deficit associated with wall cloud rotation.

b. *La Junta Colorado nonrotating wall cloud*

1) VISUAL AND DUAL-DOPPLER OBSERVATIONS

Prior to the arrival of the VORTEX2 teams in southeastern Colorado on 11 June 2009, convection was initiating over the higher terrain west and north of Pueblo, Colorado, and subsequently moved eastward. The first radar echoes associated with the La Junta supercell were observed approximately 50 km west-northwest of La Junta, Colorado, at 2251 UTC. The storm quickly became a supercell with the first tornado warning issued at 2331 UTC just west of La Junta. The La Junta supercell was tornado warned during the time of intensive VORTEX2 data collection, however, no tornadoes were confirmed.

Intensive VORTEX2 data collection began at approximately 2355 UTC. By 0019 UTC 12 June 2009,

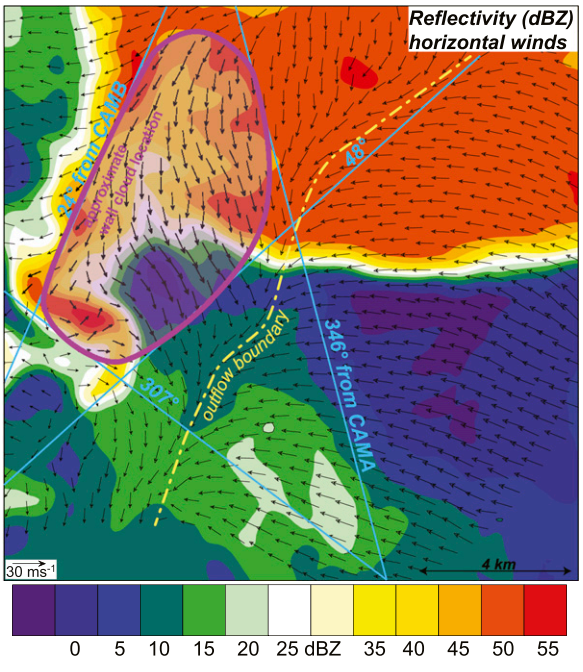

FIG. 11. Dual-Doppler data from 0018 to 0020 UTC 12 Jun 2009 at 900 m ARL are shown. Radar reflectivity from DOW 7 (color) and storm-relative winds (m s^{-1}; black vectors). Cyan lines are the left and right azimuths of the estimated wall cloud location based on photogrammetry. The thick purple line is the approximate wall cloud location. The dashed–dotted yellow line is the approximate outflow boundary location shown in Fig. 9.

supercellular convection east and southeast of Pueblo has produced an outflow boundary (Fig. 9) that is propagating to the east-southeast (not shown). The La Junta supercell updraft is located just to the west of the outflow boundary at 0019 UTC. Analysis of photos taken at the DOW6/CAMB and DOW7/CAMA sites shown in Fig. 9 reveal that a wall cloud underneath the La Junta updraft is forming at approximately 0018 UTC (Fig. 10). The wall cloud appears to be forming in the western portion of the updraft base (Fig. 10). Using the azimuths in the respective photos in Fig. 10, the triangulated wall cloud position is plotted relative to the concurrent dual-Doppler data collected by the DOW6 and DOW7 radars (Fig. 11). Much of the wall cloud is located in a region of light or no precipitation on the west side of the outflow boundary and in northerly storm-relative flow that appears to be coming from the heavy precipitation region to the north and east. Analysis of the Pueblo Weather Surveillance Radar-1988 Doppler (WSR-88D; not shown) data suggests that the northerly flow west of the outflow boundary in Fig. 11 is being augmented by outflow from the supercell north of the La Junta storm (Fig. 9).

Ten minutes later, the wall cloud at 0028:01 UTC (Fig. 12) is well defined. The wall cloud extends 800–880 m below the primary cloud base that is inferred using a nearby inflow sounding (shown later in Fig. 16). As in Fig. 10, the wall cloud base is lower to the northeast and gradually higher to the southwest.

There are noteworthy differences between the La Junta and Goshen County supercell wall clouds. First, the triangulated position of the wall cloud is not embedded in heavy precipitation (Figs. 11 and 13a). This is in contrast to the Goshen County wall cloud that is embedded in precipitation wrapping around and within the low-level mesocyclone. The La Junta wall cloud in Fig. 12 is not rotating, as observed in high-definition video (not shown). A weak low-level mesocyclone is observed in the 1.3° and 1.9° elevation scans by the Pueblo WSR-88D at altitudes of 1.7 and 2.4 km above

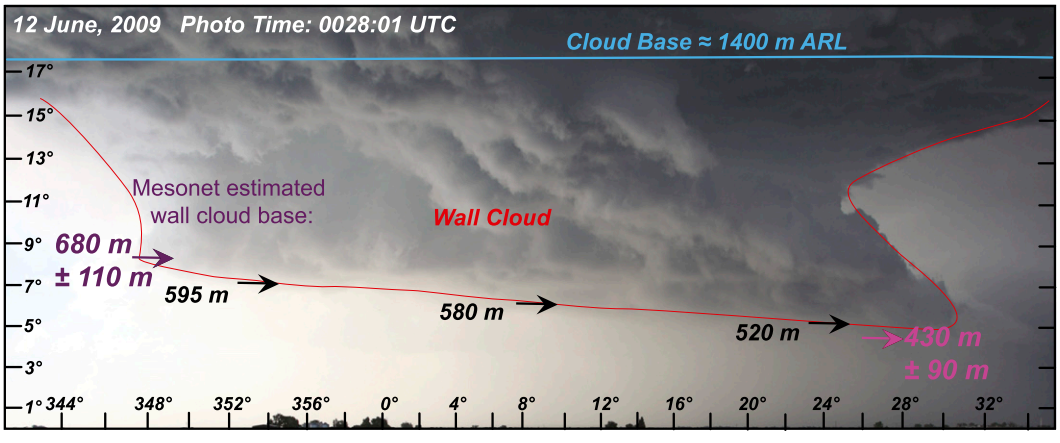

FIG. 12. Photograph of the La Junta supercell wall cloud taken at 0028:01 UTC 12 Jun 2009. Estimates of cloud-base height based on the sounding in Fig. 16 and wall cloud vertical extent estimated from photogrammetry are shown in blue and black, respectively. Mobile mesonet estimated wall cloud-base height is shown in purple and pink. Wall cloud boundary is shown in red.

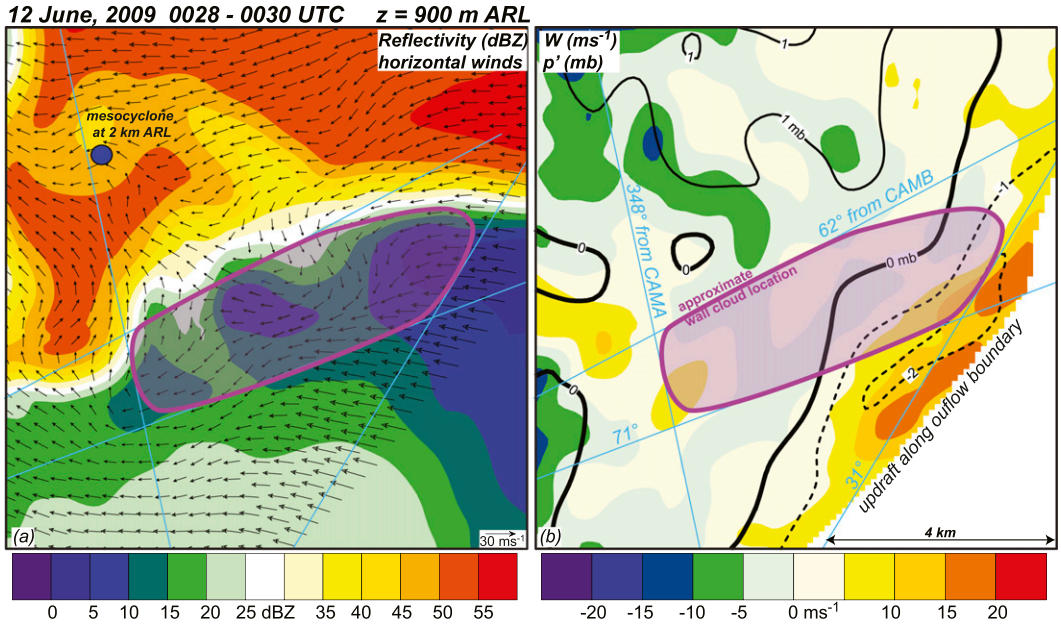

FIG. 13. Dual-Doppler data from 0028 to 0030 UTC 12 Jun 2009 at 900 m ARL are shown. (a) Radar reflectivity from DOW 7 (color) and storm-relative winds ($m\,s^{-1}$; black vectors). Cyan lines are the left and right azimuths of the estimated wall cloud location based on photogrammetry. The thick purple line is the approximate wall cloud location. (b) Vertical velocity ($m\,s^{-1}$; color) and perturbation pressure (black contours) are shown. In (b) the wall cloud location and azimuths are as in (a).

the DOW7 location, respectively. It is also observed in the dual-Doppler data at altitudes of 1.5–2.5 km ARL, but is displaced approximately 3 km to the northwest of the wall cloud (Fig. 13a). As discussed below, we hypothesize that relatively strong outflow displaced the storm's updraft from the mesocyclone. No significant pressure perturbations are evident in the wall cloud (Fig. 13b. Only weak vertical motion is observed near the wall cloud base (Fig. 13b), however, strong updraft is observed along the outflow boundary. Stronger updraft at higher levels is observed within the wall cloud region, approaching magnitudes of $20\,m\,s^{-1}$ at 2 km ARL (not shown).

2) WALL CLOUD PARCEL SOURCE REGIONS

Backward trajectories for parcels entering the wall cloud in Figs. 12 and 13 are shown in Fig. 14. The majority of the parcels entering the wall cloud originate in the forward-flank region (Figs. 14a,c). Relatively cooler (Fig. 15) parcels in the eastern portion of the forward-flank precipitation enter the lower, eastern part of the wall cloud. Relatively warmer parcels farther west (Fig. 15) enter the western, higher wall cloud. The trajectories suggest that the storm's outflow, augmented by convection to the north, is surging out ahead of the precipitation region. While some parcels travel large vertical displacements as they moved toward the wall cloud (Figs. 14b,d), the majority of the parcels ascend into the wall cloud from the forward-flank region. A few parcels appear to originate in the storm inflow (Fig. 14a), entering the eastern portion of the wall cloud from low levels (Fig. 14b).

3) WALL CLOUD FORMATION

Mobile mesonet teams successfully sampled the low-level thermodynamic properties of the forward-flank region (Fig. 15) in the area where parcels entering the wall cloud traversed. The mean potential temperature and mixing ratio values in the cooler region of the forward flank where parcels enter the eastern part of the wall cloud in Fig. 15 are approximately 301.7 K and $11.2\,g\,kg^{-1}$, respectively. These parcels saturate at approximately 430 m ARL when ascending adiabatically in the low-level updraft. This is much lower than the ambient cloud-base height estimated to be 1400 ARL by a nearby inflow sounding (Fig. 16). Farther to the southwest in the warmer portion of the forward-flank region, the mean potential temperature and mixing ratio values are 303.4 K and $10.7\,g\,kg^{-1}$, respectively. These parcels saturate at approximately 680 m ARL. Apparent in Fig. 12 is that the observed wall cloud-base heights are consistent with those estimated by lifting the forward-flank parcels in the cooler (eastern) and warmer (western) regions. The observations shown in Figs. 12–16 confirm the hypothesis that

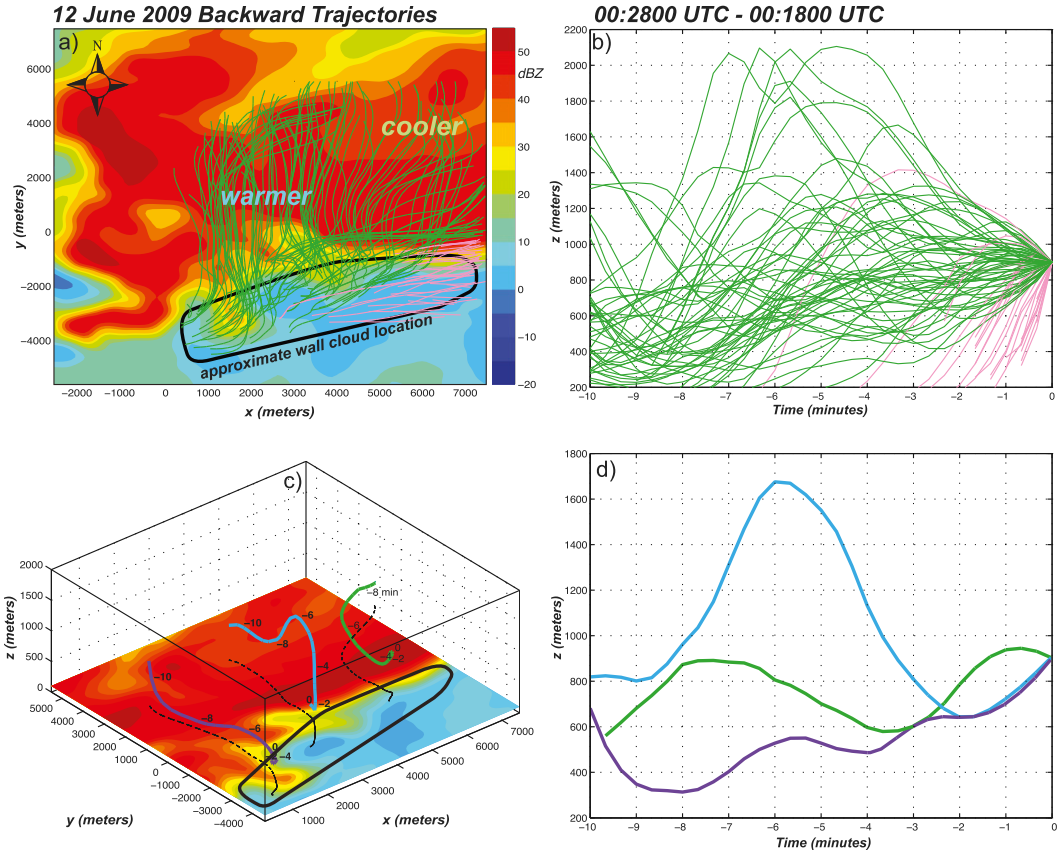

FIG. 14. Radar reflectivity from DOW 7 (color; 900 m ARL) and backward trajectories for parcels entering the wall cloud. The radar reflectivity data are from the 0028–0030 UTC dual-Doppler analysis. Backward trajectories were calculated from 0028:00 to 0018:00 UTC. (a) Plan view of radar reflectivity and trajectories. The approximate wall cloud location is shown in black. Green and pink parcel paths are from the forward-flank and inflow regions, respectively. (b) Height vs time plot of the trajectories shown in (a). (c) Three-dimensional perspective of the radar reflectivity field shown in (a) along with representative parcel trajectories. Black dashed lines represent the ground-relative location of the respective trajectories. Black time labels are minutes before the initial time of 0028:00 UTC. (d) Height vs time diagram of the three representative trajectories shown in (c).

evaporatively cooled and moistened parcels in the forward-flank region saturate below the primary cloud base in the low-level updraft creating, in this case, a nonrotating wall cloud.

4. Summary and conclusions

The formation of wall clouds associated with two supercells sampled by the VORTEX2 armada has been examined. The first supercell occurred in Goshen County, Wyoming, on 5 June 2009 producing an EF2 tornado. The Goshen County wall cloud is embedded in precipitation wrapping around and within the low-level mesocyclone. The wall cloud appears to be centered on the low-level mesocyclone and, therefore, contained significant rotation. A developing tornado is observed within the low-level mesocyclone and wall cloud. Air entering this wall cloud comes primarily from the forward-flank region of the storm. A few parcels also originate in the inflow and rear-flank downdraft. The majority of the parcels from the inflow and forward-flank regions originate at low levels. Some parcels in the forward flank originate at higher levels and descend into the wall cloud, as do the rear-flank downdraft parcels.

The notion that some parcels populating the wall cloud are descending in downdraft is perhaps not that surprising. Previous studies have shown that the low-level mesocyclone forms as horizontal vorticity is tilted by a horizontal vertical velocity gradient at the updraft–downdraft interface (RK85; Davies-Jones and Brooks 1993; Davies-Jones et al. 2001; Markowski et al. 2008). Many studies have visually observed a ''clear slot'' to wrap around the southern side of the wall cloud and tornado (if present) that has been widely accepted to be associated with subsiding air in the rear-flank downdraft [see references in Markowski (2002)]. Photogrammetry

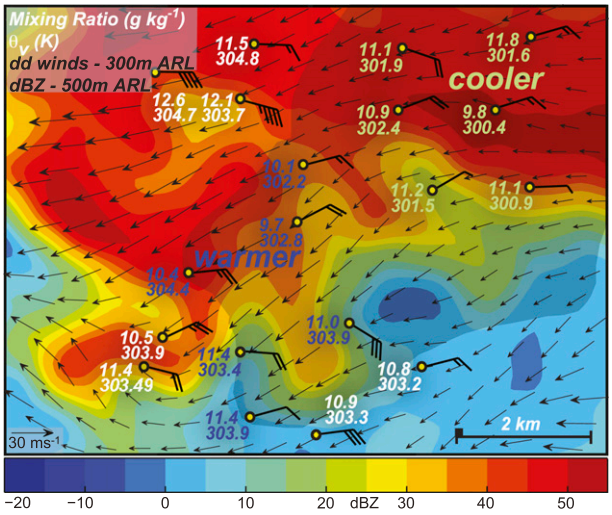

FIG. 15. Radar reflectivity from DOW 7 (color; 500 m ARL) and dual-Doppler storm-relative winds (black vectors; 300 m ARL) from the 0028:00–0030:00 UTC dual-Doppler synthesis. Mobile mesonet winds (black barbs; ½ flag = 5 m s^{-1}, full flag = 10 m s^{-1}), mixing ratio (g kg^{-1}), and potential temperature (K) are shown from 0024:00 to 0034:00 UTC. The semitransparent region represents the location of forward-flank parcel trajectories shown in Fig. 14.

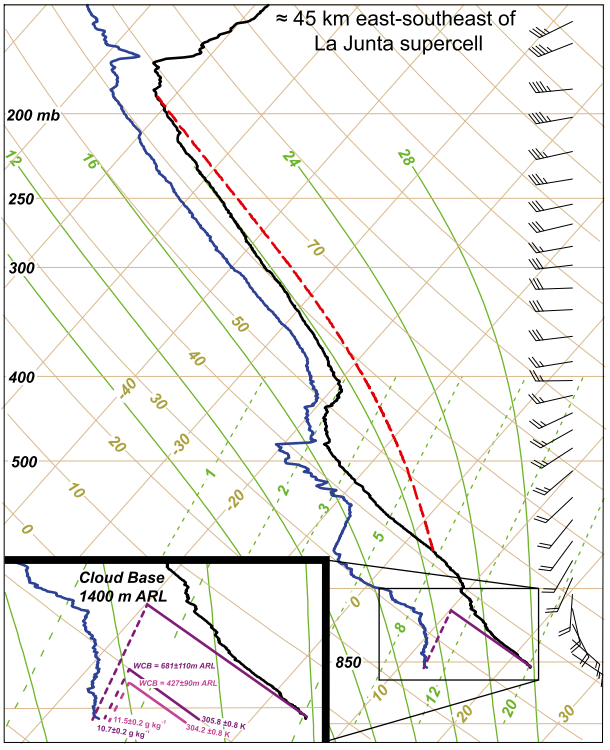

FIG. 16. NCAR GAUS sounding launched at 0014:43 UTC 12 Jun 2009 approximately 45 km to the east-southeast of the La Junta supercell. The red dashed line is the lifted parcel path. Half and full wind barbs are 5 and 10 m s^{-1}, respectively. The inset cloud-base height is based on the sounding data. The wall cloud-base (WCB) estimate is calculated from mobile mesonet observations in the warmer and cooler regions of the forward-flank region.

calculations by Golden and Purcell (1978) showed subsiding air on the south side of a tornado. Rasmussen and Straka (2007) observed downdraft in a wall cloud during the transition phase of the 2 June 1995 Dimmit, Texas, tornado. Video observations of the Goshen County wall cloud show descending cloud elements on the southern flank (not shown). It is not known how this air began to descend. High-resolution modeling and microphysical observations of the rear-flank downdraft may lead to a greater understanding of the role that the downdraft parcels play in the wall cloud evolution.

The observations show that the Goshen County wall cloud forms as low-level evaporatively cooled and moistened air in the forward-flank region ascends into the dynamically forced low-level updraft. Using mobile mesonet data to approximate the thermodynamic properties of the low-level forward-flank parcels, saturation occurs at an altitude that is consistent with the observed wall cloud base. This mechanism is consistent with that proposed by RK85. It is also shown that additional lowering is likely attributable to the cooling associated with the pressure deficit at the center of the strongly rotating wall cloud.

A well-defined wall cloud associated with a supercell west-northwest of La Junta, Colorado, on 11–12 June 2009 is examined. The La Junta wall cloud extends approximately 800–880 m below the primary cloud base and is located adjacent to the forward-flank precipitation region. The outflow, enhanced by nearby convection, appears to be surging away from the precipitation region. As a result, the wall cloud is not collocated with heavy precipitation or the low-level mesocyclone. Parcels entering the wall cloud base appear to come largely from the surging outflow. Many of the parcels originate at low levels. The La Junta wall cloud appears to form as evaporatively cooled forward-flank parcels are ingested into the low-level updraft. The wall cloud base increases from northeast to southwest. This is a result of the forward-flank downdraft being colder to the northeast. Parcel trajectories from this location of the storm enter the northeastern portion of the wall cloud saturating at a lower altitude than the warmer parcels that ascend into the southwestern portion of the wall cloud. The observed wall cloud-base height is consistent with the approximate height at which the forward-flank parcels would saturate if lifted adiabatically.

There are important similarities and differences between the conclusions of RK85 and this study concerning wall clouds. Both studies have shown that wall clouds form as evaporatively cooled air from the forward-flank region ascends into the low-level dynamically forced

updraft. This study has also shown that additional lowering may be attributed to the pressure deficit associated with strongly rotating wall clouds. Furthermore, it is shown herein that some parcels populating the wall cloud are descending from the forward-flank region and rear-flank downdraft.

Future work should examine more cases to assess the generality of these results. A modeling study would help to understand the important forcing mechanisms for parcels descending from the forward-flank region and rear-flank downdraft. It may also help to elucidate the thermodynamic structure of the boundary layer underneath wall clouds. Finally, work is under way to examine the three-dimensional structure of wall clouds and their relationship with the storm updraft, precipitation region, and low-level mesocyclone.

Acknowledgments. Research results presented herein were supported by the National Science Foundation under Grants ATM-0757714 and AGS-1242339. The DOW radars are National Science Foundation Lower Atmospheric Observing Facilities supported by ATM-0734001. The DOW deployments in VORTEX2 have been supported by ATM-0910737 and ATM-0966095. Analysis of DOW data has been supported by ATM-0947235. VORTEX2 has been supported by the National Science Foundation (ATM-0724318) and by the National Oceanic and Atmospheric Administration (NOAA). Radar data were processed with the SOLOii software maintained by the National Center for Atmospheric Research Earth Observing Laboratory. MatLab was used for trajectory visualization and analysis.

APPENDIX

Radar Sampling and Dual-Doppler Methodology

During VORTEX2, the DOWs scanned in a synchronous manner with volume updates every 2 min. The pulses were matched with lengths of 0.4 ms (60 m) and oversampled in azimuth every 0.5°. The half-power beamwidth was 0.7°. Elevation angles varied from 0.5° to 16.0° with a typical step of 1.0°.

Data were edited with SOLOii to remove noise, second trip echoes, and ground clutter. Radial velocities were unfolded. All data were rotated to correct for yaw errors using known ground clutter targets. The data were then interpolated to a Cartesian grid using a two-pass Barnes scheme (Barnes 1964). For both cases, the data spacing δ in the horizontal and vertical were calculated at the farthest range from the respective radars to the wall cloud over the analysis period. The smoothing parameter [$\kappa = (1.33\delta)^2$] (Pauley and Wu 1990) and grid spacing ($\Delta = \delta/2.5$; Koch et al. 1983) were conservatively chosen using the coarsest data spacing for all dual-Doppler analysis times. The Barnes weighting function was isotropic and was the same for all dual-Doppler synthesis times. Maximum distance from the radars to the wall cloud was 18 and 14 km for the Goshen County and La Junta wall clouds, respectively. This resulted in a horizontal and vertical grid spacing of 100 m in both cases. The horizontal grid domain was centered at the wall cloud location for all dual-Doppler volumes. The three-dimensional wind field was synthesized from the gridded radial velocities by upward integration of the anelastic mass continuity equation (Dowell and Shapiro 2003). The lower boundary condition was $w = 0$ at the lowest grid level ($z = 0$ m ARL). It was necessary to extrapolate coefficients in the dual-Doppler equations involving radial velocities and directional cosines downward to the lowest grid level in order to apply the lower boundary condition and begin the synthesis (Ray et al. 1980; Dowell and Shapiro 2003). The wind components u, v, and w were iteratively adjusted at each vertical grid level until a convergence criterion was met. All low-level extrapolated data were set to "missing" after the synthesis was complete resulting in useable data at and above 200 m ARL. The effect of hydrometeor fall speeds was neglected given the relatively small antenna elevation angles used in the synthesis.

Trajectories were computed from the dual-Doppler winds using a fourth-order Runge–Kutta integration scheme. A time step of 20 s was used. The dual-Doppler winds were assumed to vary linearly between sequential dual-Doppler analyses. Spatial interpolation was trilinear. Trajectories were not allowed to drop below the lowest level of interpolated radar data.

REFERENCES

Abrams, T., 1952: *The Manual of Photogrammetry*. George Banta Publishing, 876 pp.

Atkins, N. T., A. McGee, R. Ducharme, R. M. Wakimoto, and J. Wurman, 2012: The LaGrange tornado during VORTEX2. Part II: Photogrammetric analysis of the tornado combined with dual-Doppler radar data. *Mon. Wea. Rev.*, **140,** 2939–2958, doi:10.1175/MWR-D-11-00285.1.

Bannon, P. R., 2002: Theoretical foundations for models of moist convection. *J. Atmos. Sci.,* **59,** 1967–1982, doi:10.1175/1520-0469(2002)059<1967:TFFMOM>2.0.CO;2.

Barnes, S. L., 1964: A technique for maximizing details in numerical weather map analysis. *J. Appl. Meteor.,* **3,** 396–409, doi:10.1175/1520-0450(1964)003<0396:ATFMDI>2.0.CO;2.

Bluestein, H. B., 1983: Surface meteorological observations in severe thunderstorms. Part II: Field experiments with TOTO. *J. Climate Appl. Meteor.,* **22,** 919–930, doi:10.1175/1520-0450(1983)022<0919:SMOIST>2.0.CO;2.

——, 1984: Photographs of the Canyon, Texas, storm on 26 May 1978. *Mon. Wea. Rev.,* **112,** 2521–2523, doi:10.1175/1520-0493(1984)112<2521:POTCTS>2.0.CO;2.

——, 1993: *Synoptic-Dynamic Meteorology in Midlatitudes.* Vol. 2, *Observations and Theory of Weather Systems,* Oxford Press, 594 pp.

Davies-Jones, R. P., 1986: Tornado dynamics. *Thunderstorms: A Social and Technological Documentary.* 2nd ed. E. Kessler, Ed., Vol. 2, University of Oklahoma Press, 197–236.

——, and H. E. Brooks, 1993: Mesocyclogenesis from a theoretical perspective. *The Tornado: Its Structure, Dynamics, Prediction, and Hazards, Geophys. Monogr.,* Vol. 79, Amer. Geophys. Union, 105–114.

——, R. J. Trapp, and H. B. Bluestein, 2001: Tornadoes and tornadic storms. *Severe Convective Storms, Meteor. Monogr.,* No. 28, Amer. Meteor. Soc., 126–221.

Dowell, D. C., and A. Shapiro, 2003: Stability of an iterative dual-Doppler wind synthesis in Cartesian coordinates. *J. Atmos. Oceanic Technol.,* **20,** 1552–1559, doi:10.1175/1520-0426(2003)020<1552:SOAIDW>2.0.CO;2.

Finley, C. A., B. D. Lee, C. D. Karstens, M. Grzych, and T. M. Samaras, 2010: Mobile mesonet observations of the rear-flank downdraft evolution associated with a violent tornado near Bowdle, SD on 22 May 2010. *25th Conf. on Severe Local Storms,* Denver, CO, Amer. Meteor. Soc., 8A.2. [Available online at https://ams.confex.com/ams/pdfpapers/176132.pdf.]

French, M. M., H. B. Bluestein, I. PopStefanija, C. A. Baldi, and R. T. Bluth, 2014: Mobile, phased-array, Doppler radar observations of tornadoes at X band. *Mon. Wea. Rev.,* **142,** 1010–1036, doi:10.1175/MWR-D-13-00101.1.

Gal-Chen, T., 1978: A method for the initialization of the anelastic equations: Implications for matching models with observations. *Mon. Wea. Rev.,* **106,** 587–606, doi:10.1175/1520-0493(1978)106<0587:AMFTIO>2.0.CO;2.

Golden, J. H., and D. Purcell, 1978: Airflow characteristics around the Union City tornado. *Mon. Wea. Rev.,* **106,** 22–28, doi:10.1175/1520-0493(1978)106<0022:ACATUC>2.0.CO;2.

Grzych, M. L., B. D. Lee, and C. A. Finley, 2007: Thermodynamic analysis of supercell rear-flank downdrafts from Project ANSWERS. *Mon. Wea. Rev.,* **135,** 240–246, doi:10.1175/MWR3288.1.

Hane, C. E., and P. S. Ray, 1985: Pressure and buoyancy fields derived from Doppler radar data in a tornadic thunderstorm. *J. Atmos. Sci.,* **42,** 18–35, doi:10.1175/1520-0469(1985)042<0018:PABFDF>2.0.CO;2.

Holle, R. L., 1986: Photogrammetry of thunderstorms. *Thunderstorms: A Social and Technological Documentary,* 2nd ed. E. Kessler, Ed., Vol. 3, University of Oklahoma, 77–98.

Klemp, J. B., and R. Rotunno, 1983: A study of the tornadic region within a supercell thunderstorm. *J. Atmos. Sci.,* **40,** 359–377, doi:10.1175/1520-0469(1983)040<0359:ASOTTR>2.0.CO;2.

Koch, S. E., M. DesJardins, and P. J. Kocin, 1983: An interactive Barnes objective map analysis scheme for use with satellite and conventional data. *J. Climate Appl. Meteor.,* **22,** 1487–1503, doi:10.1175/1520-0450(1983)022<1487:AIBOMA>2.0.CO;2.

Kosiba, K., J. Wurman, Y. Richardson, P. Markowski, P. Robinson, and J. Marquis, 2013: Genesis of the Goshen County, Wyoming, tornado on 5 June 2009 during VORTEX2. *Mon. Wea. Rev.,* **141,** 1157–1181, doi:10.1175/MWR-D-12-00056.1.

Lee, B. D., C. A. Finley, and T. M. Samaras, 2011: Surface analysis near and within the Tipton, Kansas, tornado on 29 May 2008. *Mon. Wea. Rev.,* **139,** 370–386, doi:10.1175/2010MWR3454.1.

Lemon, L. R., and C. A. Doswell, 1979: Severe thunderstorm evolution and mesocyclone structure as related to tornadogenesis. *Mon. Wea. Rev.,* **107,** 1184–1197, doi:10.1175/1520-0493(1979)107<1184:STEAMS>2.0.CO;2.

Markowski, P. M., 2002: Hook echoes and rear-flank downdrafts: A review. *Mon. Wea. Rev.,* **130,** 852–876, doi:10.1175/1520-0493(2002)130<0852:HEARFD>2.0.CO;2.

——, E. Rasmussen, J. Straka, R. Davies-Jones, Y. Richardson, and R. J. Trapp, 2008: Vortex lines within low-level mesocyclone obtained from pseudo-dual-Doppler radar observations. *Mon. Wea. Rev.,* **136,** 3513–3535, doi:10.1175/2008MWR2315.1.

——, Y. Richardson, M. Majcen, J. Marquis, and J. Wurman, 2011: Characteristics of the wind field in three nontornadic low-level mesocyclones observed by the Doppler on Wheels radars. *Electron. J. Severe Storms Meteor.,* **6** (3). [Available online at http://www.ejssm.org/ojs/index.php/ejssm/article/viewArticle/75.]

——, and Coauthors, 2012a: The pretornadic phase of the Goshen County, Wyoming, supercell of 5 June 2009 intercepted by VORTEX2. Part I: Evolution of kinematic and surface thermodynamic fields. *Mon. Wea. Rev.,* **140,** 2887–2915, doi:10.1175/MWR-D-11-00336.1.

——, and Coauthors, 2012b: The pretornadic phase of the Goshen County, Wyoming, supercell of 5 June 2009 intercepted by VORTEX2. Part II: Intensification of low-level rotation. *Mon. Wea. Rev.,* **140,** 2916–2938, doi:10.1175/MWR-D-11-00337.1.

Marquis, J., Y. Richardson, J. Wurman, and P. Markowski, 2008: Single- and dual-Doppler analysis of a tornadic vortex and surrounding storm scale flow in the Crowell, Texas, supercell of 30 April 2000. *Mon. Wea. Rev.,* **136,** 5017–5043, doi:10.1175/2008MWR2442.1.

——, ——, P. Markowski, D. Dowell, J. Wurman, K. Kosiba, P. Robinson, and G. Romine, 2014: An investigation of the Goshen County, Wyoming, tornadic supercell of 5 June 2009 using EnKF assimilation of mobile mesonet and radar observations collected during VORTEX2. Part I: Experiment design and verification of the EnKF analyses. *Mon. Wea. Rev.,* **142,** 530–554, doi:10.1175/MWR-D-13-00007.1.

Moller, A. R., 1978: The improved NWS storm spotters' training program at Ft. Worth, Texas. *Bull. Amer. Meteor. Soc.,* **59,** 1574–1582, doi:10.1175/1520-0477(1978)059<1574:TINSST>2.0.CO;2.

Okubo, K., 1970: Horizontal dispersion of floatable particles in the vicinity of velocity singularities such as convergences. *Deep-Sea Res.,* **17,** 445–454, doi:10.1016/0011-7471(70)90059-8.

Pauley, P. M., and X. Wu, 1990: The theoretical, discrete, and actual response of the Barnes objective analysis scheme for one- and two-dimensional fields. *Mon. Wea. Rev.,* **118,** 1145–1163, doi:10.1175/1520-0493(1990)118<1145:TTDAAR>2.0.CO;2.

Rasmussen, E. N., and J. M. Straka, 2007: Evolution of low-level angular momentum in the 2 June 1995 Dimmitt, Texas, tornado cyclone. *J. Atmos. Sci.,* **64,** 1365–1378, doi:10.1175/JAS3829.1.

Ray, P. S., C. L. Ziegler, W. Bumgarner, and R. J. Serafin, 1980: Single- and multiple-Doppler radar observations of tornadic storms. *Mon. Wea. Rev.,* **108,** 1607–1625, doi:10.1175/1520-0493(1980)108<1607:SAMDRO>2.0.CO;2.

Richardson, Y. P., P. Markowski, J. N. Marquis, J. Wurman, K. A. Kosiba, P. Robinson, D. W. Burgess, and C. C. Weiss, 2012: Tornado maintenance and demise in the Goshen County, Wyoming supercell of 5 June 2009 intercepted by VORTEX2. *26th Conf. on Severe Local Storms,* Nashville, TN, Amer. Meteor. Soc., P13.3. [Available online at https://ams.confex.com/ams/26SLS/webprogram/Paper212526.html.]

Rotunno, R., and J. B. Klemp, 1982: The influence of the shear-induced pressure gradient on thunderstorm motion. *Mon. Wea. Rev.,* **110,** 136–151, doi:10.1175/1520-0493(1982)110<0136:TIOTSI>2.0.CO;2.

——, and ——, 1985: On the rotation and propagation of simulated supercell thunderstorms. *J. Atmos. Sci.,* **42,** 271–292, doi:10.1175/1520-0469(1985)042<0271:OTRAPO>2.0.CO;2.

Straka, J. M., E. N. Rasmussen, and S. E. Fredrickson, 1996: A mobile mesonet for finescale meteorological observations. *J. Atmos. Oceanic Technol.,* **13,** 921–936, doi:10.1175/1520-0426(1996)013<0921:AMMFFM>2.0.CO;2.

Wakimoto, R. M., N. T. Atkins, and J. Wurman, 2011: The LaGrange tornado during VORTEX2. Part I: Photogrammetric analysis of the tornado combined with single-Doppler radar data. *Mon. Wea. Rev.,* **139,** 2233–2258, doi:10.1175/2010MWR3568.1.

——, P. Stauffer, W.-C. Lee, N. T. Atkins, and J. Wurman, 2012: Finescale structure of the LaGrange, Wyoming, tornado during VORTEX2: GBVTD and photogrammetric analyses. *Mon. Wea. Rev.,* **140,** 3397–3418, doi:10.1175/MWR-D-12-00036.1.

Waugh, S., and S. E. Fredrickson, 2010: An improved aspirated temperature system for mobile meteorological observations, especially in severe weather. *25th Conf. on Severe Local Storms,* Denver, CO, Amer. Meteor. Soc., P5.2. [Available online at https://ams.confex.com/ams/25SLS/webprogram/Paper176205.html.]

Weiss, J., 1991: The dynamics of enstrophy transfer in two-dimensional hydrodynamics. *Physica,* **48,** 273–294.

Wurman, J., 2001: The DOW mobile multiple-Doppler network. *30th Int. Conf. on Radar Meteorology,* Munich, Germany, Amer. Meteor. Soc., P3.3. [Available online at https://ams.confex.com/ams/30radar/techprogram/paper_21572.htm.]

——, Y. Richardson, C. Alexander, S. Weygandt, and P. F. Zhang, 2007: Dual-Doppler and single-Doppler analysis of a tornadic storm undergoing mergers and repeated tornadogenesis. *Mon. Wea. Rev.,* **135,** 736–758, doi:10.1175/MWR3276.1.

——, K. Kosiba, P. Markowski, Y. Richardson, D. Dowell, and P. Robinson, 2010: Finescale single- and dual-Doppler analysis of tornado intensification, maintenance, and dissipation in the Orleans, Nebraska, supercell. *Mon. Wea. Rev.,* **138,** 4439–4455, doi:10.1175/2010MWR3330.1.

——, D. Dowell, Y. Richardson, P. Markowski, E. Rasmussen, D. Burgess, L. Wicker, and H. B. Bluestein, 2012: The Second Verification of the Origins of Rotation in Tornadoes Experiment: VORTEX2. *Bull. Amer. Meteor. Soc.,* **93,** 1147–1170, doi:10.1175/BAMS-D-11-00010.1.

——, K. Kosiba, and P. Robinson, 2013: In situ, Doppler radar, and video observations of the interior structure of a tornado and the wind–damage relationship. *Bull. Amer. Meteor. Soc.,* **94,** 835–846, doi:10.1175/BAMS-D-12-00114.1.

Zehnder, J. A., J. Hu, and A. Razdan, 2007: A stereo photogrammetric technique applied to orographic convection. *Mon. Wea. Rev.,* **135,** 2265–2277, doi:10.1175/MWR3401.1.